

A transformer-based deep learning approach for classifying brain metastases into primary organ sites using clinical whole brain MRI images

Qing Lyu¹, Sanjeev V. Namjoshi²⁻⁵, Emory McTyre⁴⁻⁶, Umit Topaloglu^{2,3}, Richard Barcus^{5,7}, Michael D. Chan^{2,4,6}, Christina K. Cramer^{2,4,6}, Waldemar Debinski²⁻⁴, Metin N. Gurcan^{2,9}, Glenn J. Lesser^{2,4,9}, Hui-Kuan Lin^{2,3}, Reginald F. Munden^{2,7}, Boris C. Pasche²⁻⁴, Kiran Kumar Solingapuram Sai^{2,4,5,7}, Roy E. Strowd^{2,4,9,10}, Stephen B. Tatter^{2,4,6,8}, Kounosuke Watabe^{2,3}, Wei Zhang^{2,3}, *Ge Wang¹, *Christopher T. Whitlow^{2,4-8,10,11}

Affiliations:

¹Biomedical Imaging Center, Department of Biomedical Engineering, School of Engineering, Biomedical Imaging Center, Center for Biotechnology and Interdisciplinary Studies, Rensselaer Polytechnic Institute, Troy, NY, USA

²Comprehensive Cancer Center, Wake Forest School of Medicine, Winston-Salem, NC, USA

³Department of Cancer Biology, Wake Forest School of Medicine, Winston-Salem, NC, USA

⁴Brain Tumor Center of Excellence, Wake Forest School of Medicine, Winston-Salem, NC, USA

⁵Radiology Informatics & Image Processing Laboratory, Wake Forest School of Medicine, Winston-Salem, NC, USA

⁶Department of Radiation Oncology, Wake Forest School of Medicine, Winston-Salem, NC, USA

⁷Department of Radiology, Wake Forest School of Medicine, Winston-Salem, NC, USA

⁸Department of Neurosurgery, Wake Forest School of Medicine, Winston-Salem, NC, USA

⁹Department of Internal Medicine, Wake Forest School of Medicine, Winston-Salem, NC, USA

¹⁰Department of Neurology, Wake Forest School of Medicine, Winston-Salem, NC, USA

¹¹Department of Biomedical Engineering, Wake Forest School of Medicine, Winston-Salem, NC, USA

Running title: Primary organ site classification of metastatic brain tumors

***Corresponding Authors:** Ge Wang, PhD, Rensselaer Polytechnic Institute (wangg6@rpi.edu);

Christopher T. Whitlow, MD, Wake Forest School of Medicine (cwhitlow@wakehealth.edu).

Funding: This work was supported in part by the Tumor imaging and Bioinformatics Shared Resources under the National Cancer Center Support Grant to the Comprehensive Cancer Center of Wake Forest University Health Sciences (P30CA012197). QL and GW are supported by (R01EB026646, R01CA233888, R01HL151561, R21CA264772, and R01EB031102). CW is supported by the I. Meschan Distinguished Professorship in Radiology and National Cancer Institute (P01CA207206 and P30CA012197). WZ is supported by the Hanes and Willis Professorship in Cancer. Additional support for SVN and WZ were provided by a Fellowship to WZ from the National Foundation for Cancer Research. BP is supported by the Charles L. Spurr Professorship Fund. WD is supported by the Tom and Laura Hearn Professorship for Brain Tumor Center of Excellence, and the National Cancer Institute (P01CA207206 and R01CA074145).

Conflict of interest: The authors declare no competing interests.

Authorship: Study concept and design: CW, GW, SN. Model training and analysis: QL, SN. Manuscript preparation: QL, SN, GW, CTW. Provided imaging data and performed data preprocessing: CW, RB, EM. Provided demographic data: UT. Intellectual input supervision for the study: CW, GW, WZ. Contributed to technical improvement, biological interpretation, and manuscript development: All authors.

Word count: x,xxx

Abstract:

Background: The treatment decisions for brain metastatic disease are driven by knowledge of the primary organ site cancer histology, often requiring invasive biopsy. This study aims to develop a novel deep learning approach for accurate and rapid non-invasive identification of brain metastatic tumor histology with conventional whole-brain MRI. The use of clinical whole-brain data and the end-to-end pipeline obviate external human intervention.

Methods: This IRB-approved single-site retrospective study was comprised of patients (n=1,293) referred for MRI treatment-planning and gamma knife radiosurgery from July 2000 to May 2019. Contrast-enhanced T1-weighted contrast enhanced and T2-weighted-Fluid-Attenuated Inversion Recovery brain MRI exams (n=1,428) were minimally preprocessed (voxel resolution unification and signal-intensity rescaling/normalization), requiring only seconds per an MRI scan, and input into the proposed deep learning workflow for tumor segmentation, modality transfer, and primary site classification associated with brain metastatic disease in one of four classes (lung, melanoma, renal, and other).

Results: Ten-fold cross-validation generated the overall AUC of 0.941 [95%CI:0.932,0.949], “*lung*” class AUC of 0.899 [95%CI:0.884,0.915], “*melanoma*” class AUC of 0.882 [95%CI:0.858,0.906], “*renal*” class AUC of 0.870 [95%CI:0.823,0.918], and “*other*” class AUC of 0.885 [95%CI:0.843,0.949]. It is convincingly established that whole-brain imaging features would be sufficiently discriminative to allow accurate diagnosis of the primary organ site of malignancy.

Conclusion: Our end-to-end deep learning-based radiomic method has a great translational potential for classifying metastatic tumor types using whole-brain MRI images, without additional human intervention. Further refinement may offer invaluable tools to expedite primary organ site cancer identification for treatment of brain metastatic disease and improvement of patient outcomes and survival.

Keywords: Deep learning, vision transformer, generative adversarial network (GAN), transfer learning, MRI, brain metastasis, primary organ site, classification

Key points:

1. Proposed an advanced deep learning-based radiomic method to classify brain metastases by primary organ site cancer.
2. Minimally processed clinical MRI images were used, without additional human intervention.
3. Using cutting-edge transformer-based network for automatic brain metastasis segmentation, produced high accuracy and robustness on different datasets.
4. Using cycleGAN networks for modality transfer and data fusion to predict missing modality images, enabling our method can work on incomplete data and reducing the difficulty of data collection.
5. After training, our hybrid network was systematically tested on over 1,000 patients with excellent classification results

Importance of study: In approximately 10% of cases, brain metastatic disease is the initial cancer presentation, and treatment decisions are driven by knowledge of primary organ site cancer/histologic type, which requires invasive biopsy. In this study, we develop an advanced deep learning radiomic workflow for accurate and rapid non-invasive imaging-based identification of the brain metastatic tumor histologic type using conventional T1-weighted contrast enhanced and T2-weighted-Fluid-Attenuated Inversion Recovery whole brain MRI images. The use of clinical whole-brain MRI images and the end-to-end pipeline obviate human intervention and are physician-friendly. Our results demonstrate an excellent diagnostic performance for classifying metastatic tumor types using whole-brain MRI images. Further refinement may offer invaluable

tools to expedite primary organ site cancer identification for treatment of brain metastatic disease and improvement of patient outcomes and survival.

Introduction

Approximately 180,000 patients are diagnosed with brain metastases in the US each year¹. These metastases originate from primary organ site cancers across the body, with 67%-80% originating from lung, breast, or melanoma^{2,3}. Clinical trials routinely assign treatment to patients with brain metastases based on the number and size of their brain lesions⁴, often treating all these lesions as equivalent diseases⁵. It is becoming increasingly recognized that brain metastases of different histologies have corresponding biologic behaviors and therapeutic responses. For example, it has been known for many years that melanoma brain metastases are more likely to be hemorrhagic. Breast, lung and melanoma primaries are more likely to yield multiple brain metastases, while tumors of the gastrointestinal tract are more likely to seed the posterior fossa⁶. Such patterns are readily visible on MRI examinations and have been previously noted in population studies. However, the overall sensitivity and specificity as applied to individual patients in the context of qualitative imaging evaluation of brain metastases is insufficient for definitive diagnosis/classification of the primary underlying malignancy. That being said, there are also likely biological differences between brain metastases of various histologic types that have yet to be discovered and are not evident to physicians via standard qualitative approaches. This is currently reflected within the highly granular quantitative medical imaging data, and can be leveraged for sensitive and specific classification into brain metastatic disease histologic types. Our overall hypothesis is that imaging features of brain metastases are sufficiently discriminative and may be detected by radiomics at the time of initial evaluation to allow accurate diagnosis of the primary organ site cancer.

In approximately 10% of cases, brain metastatic disease is the initial cancer presentation⁷, and treatment decisions are driven by knowledge of the primary organ site/histologic type. In these cases, an oncologic workup including cross-sectional imaging of the remainder of the body may identify the most likely primary organ site. If a primary malignancy site is identified that is amenable to biopsy, then tissue is often obtained directly from that extracranial site to confirm the

histologic diagnosis. If there are no extra-cranial sites amenable to biopsy, and the brain metastatic disease is in a favorable location, then invasive intracranial tissue sampling may be necessary for definitive diagnosis. Often, the specific treatment recommended for brain metastatic disease hinges on knowing the primary organ site of the malignancy, which underscores the important and immediate need to develop a non-invasive methodology that can conclusively identify the primary organ site of brain metastatic disease to facilitate rapid management and optimize treatment decision.

Deep learning-based radiomics, as an emerging field uses deep learning-based algorithms to transfer standard medical images into high-dimensional quantitative features, have led to new tools capable of recognizing features in medical imaging data that may not be easily perceived by physicians, such as radiologists⁸. Radiomic tools have been applied to quantitative image analysis and expedite the clinical diagnosis of cancer⁸⁻¹⁰. To date, physicians who use diagnostic imaging for neuro-oncology evaluation, such as radiologists and oncologists, are generally unable to determine the primary organ site of cancer from images of brain metastases alone. However, it is possible to use radiomic tools to identify the primary organ site of brain metastases by leveraging patterns or features within medical imaging data¹¹. Previously, radiomic tools utilized dedicated algorithms to extract handcrafted features. As a result, only a limited number of heuristic features are available. Although such a problem can be alleviated with the image transform like wavelet transform¹¹, the scope of extracted features is still limited. Deep learning, as the mainstream of artificial intelligence, is a data-driven approach, holding a great promise to address this challenge. Recently, deep learning has been widely used in radiomics for many tasks, such as cancer prognostication and cancer radiotherapy failure rate prediction^{12,13}. Recently, deep learning has also achieved a great success in recognizing primary or metastasis tumors and classifying metastasis tumors into their origins based on whole-slide histological images¹⁴.

We hypothesized that deep learning-based radiomics, or deep radiomics, could identify the primary organ site cancer associated with a patient's brain metastatic disease using clinical MRI images. Furthermore, we hypothesized that the classification process could be expedited with minimal image preprocessing in an automated workflow that requires minimal human intervention/feature engineering. Here we report a deep radiomic approach for classification of the primary organ site of brain metastases based on 3D structural MRI T1 and/or T2-weighted images.

Figure 1 shows an overview of our study design. Two big datasets were clinically collected consisting of 1,293 subject with 1,428 cases respectively. The images with tumor contours were used for training and validation of our tumor segmentation network. Once trained, pixel-wise tumor possibility maps were generated by the tumor segmentation network. Subjects with both T1-weighted contrast enhanced (T1 CE) and T2-weighted-Fluid-Attenuated Inversion Recovery (T2 FLAIR) were used to train a cycleGAN¹⁵ in the weakly supervised learning mode to transfer image modalities between T1 CE and T2 FLAIR. After training, either a T1 CE or T2 FLAIR image can be used to produce the image in the complementary modality (that is, either the corresponding T2 FLAIR or T1 CE image). Finally, we used all cases, each case's modality transferred case, and corresponding tumor possibility maps into our classification network for inferencing the primary organ site of brain metastases. Once trained, the whole workflow can be implemented in an end-to-end way.

Results

Patient demographic analysis

Two big datasets with a total of 1,293 subjects (mean \pm SD age, 62.77 ± 11.86 years, 63.57% male) were used. Specifically, for the dataset with tumor contours, there were 148 subjects (61.77 ± 11.15 years; 56.85% male); and for the dataset without tumor contours, there

were 1,145 subjects (62.85 ± 11.91 years; 64.54% male). Specifically, the “*lung*” category had 801 subjects (63.21 ± 11.06 years; 54.93% male), “*melanoma*” category had 313 subjects (62.80 ± 13.81 years; 72.20% male), “*renal*” category had 82 subjects (62.47 ± 11.16 years; 85.37% male), and “*other*” category had 97 subjects (59.81 ± 12.25 years; 82.47% male). In the dataset with tumor contours, 54.11% patients/scans had 1-3 lesions (mean \pm SD = 4.79 ± 5.27).

Tumor segmentation

To conduct deep radiomic analysis, it is necessary to label targets and extract their features. In this study, we adapted a U-Net-shaped network with transformers in the bottleneck for tumor segmentation. The proposed segmentation network segments brain metastasis tumors and generates pixel-wise tumor possibility maps to guide the proposed classification network to pay due attention on metastases. The proposed networks were trained on T1 CE and T2 FLAIR dataset separately. Figure 2e-g compares our proposed method with other brain tumor segmentation networks. Different from the other methods, our proposed network has two major merits: 1) high sensitivity on both smaller and larger metastases, 2) high robustness over different datasets.

For the brain metastasis segmentation, one major challenge is a strong heterogeneity of tumor sizes. Some small metastasis tumors only account for a few pixels in an MRI image, which can be easily neglected by generic networks since information can be lost during a down-sampling process. On the other hand, how to precisely segment a large tumor is also difficult because convolutional neural networks (CNN) tend to focus more on local features. To address this problem, we proposed a novel network synergizing both convolutional layers and transformers. In contrast to convolutional layers, transformers focus on global information via a self-attention mechanism. The combination of locally oriented convolutional layers with transformers with global awareness guarantees that the proposed network integrates both local and contextual features. In addition, the skip connections are made between down-sampling and up-sampling blocks to

minimize the information loss in the feature extraction process. By this architectural design, our proposed network has inherent capabilities of segmenting both small (e.g. the tumor pointed by a yellow arrow in Figure 2g) and large metastasis tumors (e.g. the tumor pointed by a red arrow in Figure 2g) equally well. Interestingly, in some cases, segmented results even outperform human labeled results, as the tumor pointed by the green arrow in Figure 2f.

The other major merit of the proposed segmentation network is its robustness and generalizability over different datasets. When testing on data without tumor contours, the proposed network behaved quite conservatively to avoid false positive prediction (Figure 2g). This characteristic is of critical importance in the clinical setting. As MRI images are collected from scanners manufactured by different manufacturers, it is impractical to have every MRI case collected under the same protocol and techniques. A robust network can tolerate the conditional differences in the data collection process and generalize well on different datasets.

Modality transfer

In this study, we hoped to use both of T1 CE and T2 FLAIR images for tumor classification so that complementary features can enhance the radiomic analysis. However, as in most medical imaging projects, it is challenging to collect big data meeting all our requirements. Instead, there were only 127 subjects with both T1 CE and T2 FLAIR scans, and these images are not strictly paired in terms of the slice position and were collected in different time points. Given these facts, we developed a cycleGAN in a weakly supervised way for modality transfer; that is to generate missing modality images.

In our experiments, 125 subjects with both T1 CE and T2 FLAIR cases were randomly selected for training and the other two subjects for validation. Figure 3a shows the workflow for cycleGAN training. Mutual information was minimized to find the most similar image in the target modality MRI case to form pairs. Figure 3b shows modality transfer results on both a validation dataset and two cases without its corresponding modality. It is found that cycleGAN can generate

modality transferred results in a style very similar to that of their targets. The generated modality transferred results were more realistic than results from that using the style transfer method¹⁶ as shown in Supplementary Figure 1. We tested cycleGAN on each subject only with either T1 CE or T2 FLAIR images to generate the missing modality image, which were used so that our classification network has always T1 CE and T2 FLAIR images as the input.

Four-class classification

Using the proposed tumor segmentation network and cycleGAN, we obtained a set of data for each MRI scan: the original MRI scan in the either T1 CE or T2 FLAIR contrast mechanism, its corresponding missing modality data, and pixel-wise tumor possibility map. We feed these images and map to the classification network for predicting the primary organ site of brain metastases. Figure 4c,e-f show our 10-fold classification results. The overall AUC is 0.941 with 95% confidence interval of 0.932 and 0.949; “*lung*” class AUC is 0.899 with 95% confidence interval of 0.884 and 0.915; “*melanoma*” class AUC is 0.882 with 95% confidence interval of 0.858 and 0.906; “*renal*” class AUC is 0.870 with 95% confidence interval of 0.823 and 0.918; and “*other*” class AUC is 0.885 with 95% confidence interval of 0.843 and 0.949.

To investigate the contribution of adding tumor prediction maps to the performance of the classification network, we conducted an ablation study without involving tumor prediction maps. It can be observed in Figure 4d that adding tumor classification maps greatly improved the overall AUC score by 4.1%. Meanwhile, another ablation study was performed only using T1 CE or T2 FLAIR images. As shown in Figure 4d, removal of either T1 CE or T2 FLAIR images decreased the overall AUC by 5.4% and 8.1%, respectively.

Discussion

Brain metastases are common often as an initial presentation of lung cancer, melanoma, and renal cancer^{17,18}. Of those who develop brain metastases, 36% are diagnosed within 1-month

of the initial presentation and 72% are diagnosed within the first year¹⁹. Survival of patients presenting with brain metastatic disease is poor, with a median survival of 3.7 months and worse particularly for patients with lung cancer²⁰. Factors associated with more favorable survival for these patients of brain metastatic disease include use of appropriate systemic therapy for better performance status²¹. Critical to initiation of optimal systemic therapy is establishing an accurate diagnosis of the primary organ site. Of particular importance is not delaying initiation of brain-directed treatment with extensive systemic imaging studies, diagnostic biopsies, or other methods for the primary organ site identification²²⁻²⁴. To this end, our work presents a deep learning-based radiomic pipeline for easy and conclusive identification of the most common primary organ sites for brain metastatic disease using clinically acquired T1 CE or T2 FLAIR whole brain MRI images alone, thus opening the door for rapid translation into clinical care. Owing to the end-to-end nature, the proposed framework is user friendly and can be implemented within seconds with minimal human intervention. To our best knowledge, this study represents the first application of deep learning to extract radiomic features for this critically important classification task, and the cross-validation approach suggests that the results are generalizable.

Our results further demonstrate that the deep learning approach is feasible and could be improved with a larger image dataset. We achieved the highest accuracy on the “*lung*” category, which took the majority (61.83%) of all cases used in this study. Since deep learning is data-driven, the network can better learn how to extract radiomic features for analysis with more cases involved in the training process. Within one month after the publication of this paper, we will open our codes for federated learning, and continuously add more whole-brain MRI cases into the proposed radiomic pipeline to further improve the classification performance.

The inclusion of cycleGAN in the proposed radiomic pipeline relaxes the requirement for clinical translation. Clinically, it is rare to have a large batch of datasets with each subject scanned in multiple MRI modalities. A common scenario is that an individual subject is scanned with only a single modality. The use of cycleGAN for modality transfer generates missing modalities

semantically, overcoming the difficulty of data collection and making the proposed method widely applicable. Meanwhile, more single modality cases can be capitalized via modality transfer in the training process to improve classification results. As shown in Figure 4d, compared with using either T1 CE or T2 FLAIR alone, the dual-modality input via modality transfer led to significantly higher AUC scores.

There are several opportunities for further improvements of our deep learning model. First, additional medical images from the primary cancer site should be helpful in the proposed radiomic pipeline, such as lung CT images. We hypothesize that there may be some common or correlated deep radiomic features between tumors in the primary site and the brain. Adding these additional images may guide the network to find these common or correlated features for better classification. While MRI is uncommon in certain body regions, there are already efforts underway to supplement patient screening in domains currently dominated by radiography and CT²⁵. Second, with a greater number of images, it will be possible to increase the number of classes and cover more histological subtypes. Brain metastases originating from different subtypes may have differential responses to certain targeted treatments and immunotherapies, and a finer-grained classification scheme may be necessary to elucidate these differences. For example, Lu *et. al.* divided metastasis into 18 categories based on 32,537 whole-slide images¹⁴. Third, to obtain more data for deep learning, the partnership or consortium is important among multiple institutions and hospitals. To address the concern over privacy and ownership of medical data, one promising solution is federated learning²⁶. Fourth, further iterations on our model will be needed to diagnose patients with cancer of unknown primary, which may remain unknown until death in some cases. Hopefully, we will refine our model in the future to further analyze patients with cancer of unknown primary for the primary etiology so that optimal therapies can be initiated in a timely manner. We had initially sought to test our model on cancer of unknown primary; however, there were too few cases in our cohort ($n < 21$).

Using deep learning to extract radiomic features has shown a great potential to outperform handcrafted radiomic analyses^{11,27}. For this brain metastasis classification, beyond the previous hand-crafted feature-derived results, our approach has produced significantly better AUC scores in performing multi-class classification (0.941 vs 0.873). Unlike conventional radiomics relying on limited handcrafted features like gray-level co-occurrence and run-length metrics, deep radiomics does not rely on pre-defined algorithms, instead it learns how to extract radiomic features by itself. For conventional radiomics, one typical scenario is that if handcrafted features are not adequately extracted, radiomics cannot obtain good results. Such a problem can be solved by deep radiomics through data-driven learning. Although it is in principle that deep learning-based radiomics is superior to conventional methods, there is no need to discard conventional radiomics. A synergistic way is to combine conventional handcrafted features extraction with deep radiomics. While deep radiomics is automatic and systematic, handcrafted features have clearer meanings and rich semantics. In other words, learned and handcrafted features may help each other to boost the diagnostic performance.

Last but not the least, deep learning-mediated classification of the primary organ site cancer associated with brain metastatic disease could improve outcomes in the setting of healthcare disparities. According to a recent CDC study, 263,054 adult respondents to a survey in the United States came from rural counties²⁸. These counties generally have less access to healthcare, with hospitals that may be understaffed and lacking the equipment to perform specialized diagnostic tests. Such health disparities have resulted in poorer health status and quality of life, as compared to the general population. Indeed, Renz et al.²⁹ noted that rural location is a predictor for increased death, as well as compromised whole brain radiation therapy outcomes for squamous cell carcinoma brain metastases. An algorithm like the one described in this paper, once properly trained and validated, can be deployed online to process images in real-time as a tool for radiologists and oncologists, to improve workflow and diagnosis. This would allow lower cost, fewer tests, and faster determination of the primary organ site of brain

metastases, as well as less healthcare disparities. Collectively, our results show the potential of the deep learning approach that will have a widespread impact on the diagnosis and treatment of brain metastases to improve healthcare outcomes and quality of life for patients.

Acknowledgements

We would like to thank Nikita Namjoshi and Josh Tan for comments and suggestions. We would also like to thank Drs. Guangxu Jin and Liang Liu with Wake Forest Baptist Comprehensive Cancer Center Bioinformatics Shared Resource for their inputs.

References

1. Ellis, T.L., Neal, M.T. & Chan, M.D. The role of surgery, radiosurgery and whole brain radiation therapy in the management of patients with metastatic brain tumors. *Int J Surg Oncol* **2012**, 952345 (2012).
2. Nayak, L., Lee, E.Q. & Wen, P.Y. Epidemiology of brain metastases. *Curr Oncol Rep* **14**, 48-54 (2012).
3. Vuong, D.A., Rades, D., Vo, S.Q. & Busse, R. Extracranial metastatic patterns on occurrence of brain metastases. *J Neurooncol* **105**, 83-90 (2011).
4. Devoid, H.M., *et al.* Recent advances in radiosurgical management of brain metastases. *Front Biosci (Schol Ed)* **8**, 203-214 (2016).
5. Brown, P.D., *et al.* Effect of Radiosurgery Alone vs Radiosurgery With Whole Brain Radiation Therapy on Cognitive Function in Patients With 1 to 3 Brain Metastases: A Randomized Clinical Trial. *JAMA* **316**, 401-409 (2016).
6. Delattre, J.Y., Krol, G., Thaler, H.T. & Posner, J.B. Distribution of brain metastases. *Arch Neurol* **45**, 741-744 (1988).
7. Waqar, S.N., *et al.* Brain Metastases at Presentation in Patients With Non-Small Cell Lung Cancer. *Am J Clin Oncol* **41**, 36-40 (2018).
8. Lambin, P., *et al.* Radiomics: the bridge between medical imaging and personalized medicine. *Nature reviews Clinical oncology* **14**, 749-762 (2017).
9. Fass, L. Imaging and cancer: a review. *Mol Oncol* **2**, 115-152 (2008).
10. Gillies, R.J., Kinahan, P.E. & Hricak, H. Radiomics: Images Are More than Pictures, They Are Data. *Radiology* **278**, 563-577 (2016).
11. Kniep, H.C., *et al.* Radiomics of brain MRI: utility in prediction of metastatic tumor type. *Radiology* **290**, 479-487 (2019).
12. Hosny, A., *et al.* Deep learning for lung cancer prognostication: a retrospective multi-cohort radiomics study. *PLoS medicine* **15**, e1002711 (2018).
13. Lou, B., *et al.* An image-based deep learning framework for individualising radiotherapy dose: a retrospective analysis of outcome prediction. *The Lancet Digital Health* **1**, e136-e147 (2019).
14. Lu, M.Y., *et al.* AI-based pathology predicts origins for cancers of unknown primary. *Nature* **594**, 106-110 (2021).
15. Zhu, J.-Y., Park, T., Isola, P. & Efros, A.A. Unpaired image-to-image translation using cycle-consistent adversarial networks. in *Proceedings of the IEEE international conference on computer vision* 2223-2232 (2017).
16. Gatys, L.A., Ecker, A.S. & Bethge, M. Image style transfer using convolutional neural networks. in *Proceedings of the IEEE conference on computer vision and pattern recognition* 2414-2423 (2016).
17. Fox, B.D., Cheung, V.J., Patel, A.J., Suki, D. & Rao, G. Epidemiology of metastatic brain tumors. *Neurosurg Clin N Am* **22**, 1-6, v (2011).
18. Gavrilovic, I.T. & Posner, J.B. Brain metastases: epidemiology and pathophysiology. *J Neurooncol* **75**, 5-14 (2005).
19. Schouten, L.J., Rutten, J., Huveneers, H.A. & Twijnstra, A. Incidence of brain metastases in a cohort of patients with carcinoma of the breast, colon, kidney, and lung and melanoma. *Cancer* **94**, 2698-2705 (2002).
20. Berk, L. & Stevens, B. Outcome of patients with an initial presentation of brain metastases. **32**, 133-133 (2014).
21. Ferreira Dos Santos, V.M., *et al.* Brain metastasis as initial presentation of lung cancer - Impact of prognostic factors on patient survival. **50**, PA4232 (2017).

22. Polyzoidis, K.S., Miliaras, G. & Pavlidis, N. Brain metastasis of unknown primary: a diagnostic and therapeutic dilemma. *Cancer Treat Rev* **31**, 247-255 (2005).
23. Koc, Z.P., Kara, P.O. & Dagtekin, A. Detection of unknown primary tumor in patients presented with brain metastasis by F-18 fluorodeoxyglucose positron emission tomography/computed tomography. *CNS Oncol* **7**, CNS12 (2018).
24. Han, H.J., *et al.* Optimal Treatment Decision for Brain Metastases of Unknown Primary Origin: The Role and Timing of Radiosurgery. *Brain Tumor Res Treat* **4**, 107-110 (2016).
25. Biederer, J., *et al.* MRI of the lung (3/3)-current applications and future perspectives. *Insights Imaging* **3**, 373-386 (2012).
26. Dayan, I., *et al.* Federated learning for predicting clinical outcomes in patients with COVID-19. *Nature Medicine*, 1-9 (2021).
27. Ortiz-Ramón, R., Larroza, A., Ruiz-España, S., Arana, E. & Moratal, D. Classifying brain metastases by their primary site of origin using a radiomics approach based on texture analysis: a feasibility study. *European radiology* **28**, 4514-4523 (2018).
28. James, C., *et al.* Racial/Ethnic Health Disparities Among Rural Adults — United States, 2012–2015. in *MMWR Surveill Summ* 2017, Vol. 66 1-9 (2017).
29. Renz, P., Hasan, S. & Wegner, R.E. Survival outcomes after whole brain radiotherapy for brain metastases in older adults with newly diagnosed metastatic small cell carcinoma: A national cancer database (NCDB) analysis. *J Geriatr Oncol* (2019).
30. Lyu, Q., Shan, H. & Wang, G. MRI super-resolution with ensemble learning and complementary priors. *IEEE Transactions on Computational Imaging* **6**, 615-624 (2020).
31. Mao, X., *et al.* Least squares generative adversarial networks. in *Proceedings of the IEEE international conference on computer vision* 2794-2802 (2017).

Materials and Methods

Data acquisition and processing

For this IRB-approved single-site retrospective patient study, our initial dataset consists of 1,862 conventional treatment-planning MRI scans from 1,650 subjects imaged at Wake Forest School of Medicine from July 13, 2000, to May 2, 2019, who were referred for Gamma Knife Radiosurgery. This study used structural MRI images with patients in a stereotactic head frame as part of the clinical GK treatment planning routine on the following scanners: 1.5T General Electric SIGNA Excite (GE Healthcare), 1.5T General Electric SIGNA HDxt (GE Healthcare), 3.0T General Electric SIGNA Excite (GE Healthcare), and 3.0T Siemens Skyra (Siemens Medical Solutions). The voxel sizes varied from approximately 0.5 x 0.5 x 2 mm to 0.5 x 0.5 x 3 mm, depending on scanners/protocols.

Image labeling and pre-processing

Clinical labels to the MRI images were extracted from the electronic medical records, including tissue biopsy proven pathologic diagnoses. In total, there are 77 diagnostic categories for all the images. Apart from lung cancer, melanoma, and renal cancer, all other diagnostic labels were pooled together into an “Other” class. In other words, this labeling strategy defines four classes. All the images associated with a biopsy-proven diagnosis were included for network training.

Our images were collected in two batches: one batch of images had human labeled brain metastasis tumor contours, and the other batch of images were not processed and associated with no tumor contour. The original dataset with tumor contours contains 148 subjects (Male: 83, Female: 65) with 360 cases (T1 CE: 171, T2 FLAIR: 189). In each case, tumor contours were manually labeled by experienced radiologists. Images were stored in the Dicom format, with the tumor contours stored in RTSTRUCT files. To create brain metastasis tumor segmentation labels, it is necessary to register tumor contours with the corresponding MR images, since the contours

do not match the tumors well due to some minor technical incompatibilities. Hence, we utilized an affine transformation to implement tumor contour registration and created tumor masks as the labels to train our segmentation network. After the registration between the contours and the tumors, 77 cases were removed due to signal degradation, motion blurring, and other artifacts. In most of these failure cases, the main reason is the fading or diminishing of metastases after radiotherapy. There are 1,502 subjects (Male: 981, Female: 521) in the dataset without tumor contours. Each subject was only scanned once. In this dataset, 136 cases were first excluded because they are neither T1 CE or T2 FLAIR. Then, additional 221 cases were removed because they failed to cover the whole brain or there were severe image quality issues. After exclusion of the inappropriate cases, 1,428 cases from 1,293 subjects were selected for this study. Among them, 283 cases (T1 CE: 138, T2 FLAIR: 146) were with tumor labels. For each case, we unified voxel resolution via linear interpolation and normalized intensity distributions using Advanced Normalization Tools (ANTs, <https://github.com/ANTsX/ANTs>).

Training and validation datasets

For tumor segmentation, we only utilized images with tumor contours for network training and validation. We randomly selected 120 T1 CE cases and 125 T2 FLAIR cases for training. The other 18 T1 CE cases and 20 T2 FLAIR cases were used for validation. Specifically, the proposed tumor segmentation network was trained on T1 CE and T2 FLAIR images respectively. After training, all the cases used in this study were processed to generate the corresponding tumor possibility maps in the sense of Softmax.

To perform the modality transfer between T1 CE and T2 FLAIR images, we used 254 cases (T1 CE: 127, T2 FLAIR: 127) from 127 subjects to train and validate the modality transfer network. 250 cases from 125 subjects were randomly selected for the training and the other 4 cases from the remaining 2 subjects for validation. After training and validation, all the cases were processed to generate the modality transferred images.

For the tumor classification, we utilized the 10-fold cross-validation scheme on all the cases used in this study involved in the training and validation stage. The classification results shown in this paper are based on the average data of 10 cross-validation runs.

Tumor segmentation network design

In this study, we proposed an advanced network for brain tumor detection by combining convolutional layers for local feature extraction and transformers for global awareness. The proposed network is in the U-Net structure. As shown in many other deep learning tasks, adopting the U-Net demands a reasonable computational cost and delivers the decent network performance. The structure of the proposed segmentation network is illustrated in Figure. 2a-d.

The proposed network includes the four components: a down-sampling convolutional branch, a transformer-based bottleneck, an up-sampling convolutional branch, and skip connections between the down-sampling and up-sampling branches. The down-sampling branch contains ten down-sampling blocks. In each down-sampling block, there are two arms, the first arm has three convolutional layers followed by group normalization and ReLU activation. Down-sampling happens in the second convolutional layer with a stride of two. The second arm only has one convolutional layer with a stride of two. Feature maps from the two arms are finally added together. In the up-sampling branch, there are five up-sampling blocks. Each up-sampling block contains two convolutional layers followed by group normalization and ReLU activation. An up-sampling layer is then added to expand the feature maps by a factor of two. There are skip connections between each pair of down-sampling and up-sample blocks. The bottleneck consists of twelve identical transformers. Before feeding feature maps to the first transformer encoder, feature maps are vectorized into a series of 1D tokens. Combining convolutional layers and transformers ensures that the network would utilize both local and global information. For more details, please see Supplementary Table 1.

The objective function of the proposed segmentation network combines cross-entropy and Dice loss:

$$\min_S \mathcal{L} = 0.5 \text{ cross_entropy} + 0.5 \text{ Dice} \quad (1)$$

where S is the parameters of the proposed segmentation network.

Modality transfer network design

CycleGAN¹⁵ has shown great successes in image style transfer and other tasks. It uses a generative adversarial mechanism in the training process to let the generator learn the real distribution of target data. Meanwhile, the adoption of the cycle consistency loss avoids the contradiction in adversarially generated images, and the resultant cycleGAN network can be trained in a weakly supervised fashion. We used cycleGAN for modality transfer in this study. The proposed cycleGAN has two identical generators and two identical discriminators, as shown in Figure 3a. Generator 1 was designed to transform T1 CE images to T2 FLAIR counterparts, and Generator 2 was expected to generate T1 CE images from T2 FLAIR counterparts. Discriminators 1 and 2 judge the generated T1 CE or T2 FLAIR images are true or not. The generators and discriminators are of the same structures as those described in our recent work³⁰

In the training process, mutual information is used to find the most similar slice from the corresponding modality scan of the same patient so that the network can be trained in a weakly supervised way. We use the least-square adversarial loss³¹ in the training process. The objective function for the two generators is as follows:

$$\min_G \mathcal{L} = \mathcal{L}_{adv} + \lambda \mathcal{L}_{cyc} \quad (2)$$

$$\mathcal{L}_{adv} = \mathbb{E}_x(D_1(G_1(x)) - 1)^2 + \mathbb{E}_y(D_2(G_2(y)) - 1)^2 \quad (3)$$

$$\mathcal{L}_{cyc} = \mathbb{E}_x(G_2(G_1(x)) - x)^2 + \mathbb{E}_y(G_1(G_2(y)) - y)^2 \quad (4)$$

where G and D stand for Generator and Discriminator respectively, \mathcal{L}_{adv} is the adversarial loss, and \mathcal{L}_{cyc} is the cycle consistency loss. The objective functions of the two generators are:

$$\min_{D_1} \mathcal{L} = \mathbb{E}_x(D_1(G_1(x)) - 0)^2 + \mathbb{E}_y(D_1(y) - 1)^2 \quad (5)$$

$$\min_{D_2} \mathcal{L} = \mathbb{E}_y(D_2(G_2(y)) - 0)^2 + \mathbb{E}_x(D_2(x) - 1)^2. \quad (6)$$

Tumor classification network design

The proposed tumor detection network consists of two identical feature extraction branches, where the possibility maps are gradually down-sampled via 3D maximum pooling and finally concatenated with the features from the two branches. There is an attention module to combine the features extracted from T1 CE and T2 FLAIR branches. Then, two fully connected layers are used to generate the final classification outcome. Each feature extraction branch works through a 3D convolutional layer and five subsequent down-sampling blocks. The down-sampling blocks share the same structure as that in the segmentation network. The only difference lies in that 2D convolutional layers are upgraded to 3D convolutional layers. The attention module consists of a channel attention branch and a spatial attention branch. In the channel attention branch, feature maps are first converted into vectors via 3D global averaging, then two fully connected layers calculate the weight for each channel, and finally feature maps are channel-wise multiplied by channel weights. In the spatial attention branch, feature maps are first channel-wise averaged, the weight in each voxel is determined via sigmoid activation, and finally feature maps are voxel-wise multiplied by weights. The outputs of the channel attention and spatial attention branches are element-wise added to form new feature maps. The objective function of the proposed classification network is the weighted cross-entropy. The proposed classification network are further detailed in Supplementary Table 2.

Implementation details

We used the Adam optimizer to train the segmentation, modality transfer, and classification networks respectively. For the segmentation network, the batch size was set to 12

per GPU. The learning rate was $1e-4$. The training stopped when there was no significant (less than 1%) loss decay for 20 epochs. For the modality transfer network, the batch size was 1 per GPU. The training continued 50 epochs with a learning rate of $1e-4$. For the classification network, the batch size was set to 3 per GPU. The learning rate was set to $1e-5$ in the first 50 epochs and then divided by a factor of 2 after every 10 epochs. The training stopped when there was no significant loss decay for 20 epochs. All experiments were conducted on 8 Nvidia Tesla V100 GPU with 32 GB memory.

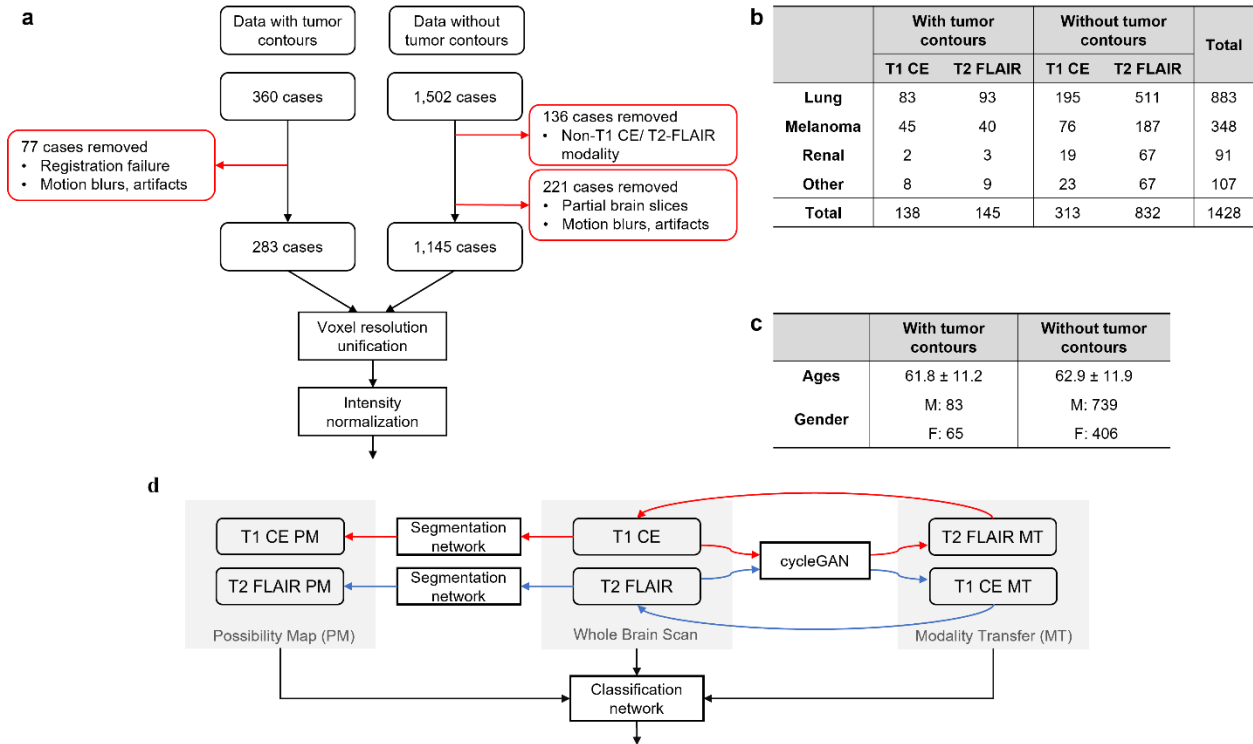


Fig. 1: Proposed deep radiomic workflow and data characteristics. (a) Statistics of the 1,428 cases collected for this study; (b) Statistics of the 1,293 subjects used in this study; and (c) flowchart of the proposed deep learning-based pipeline for brain metastasis classification, where a pre-processed T1 CE or T2 FLAIR whole-brain MRI image volume is first input a cycleGAN for modality transfer to synthesize the corresponding missing modality MRI image volume, then the pair of the images are analyzed by a tumor segmentation network to generate pixel-wise tumor possibility maps, and finally the original and synthesized images as well as associated possibility maps are fed to a classification network to predict the origin of brain metastases.

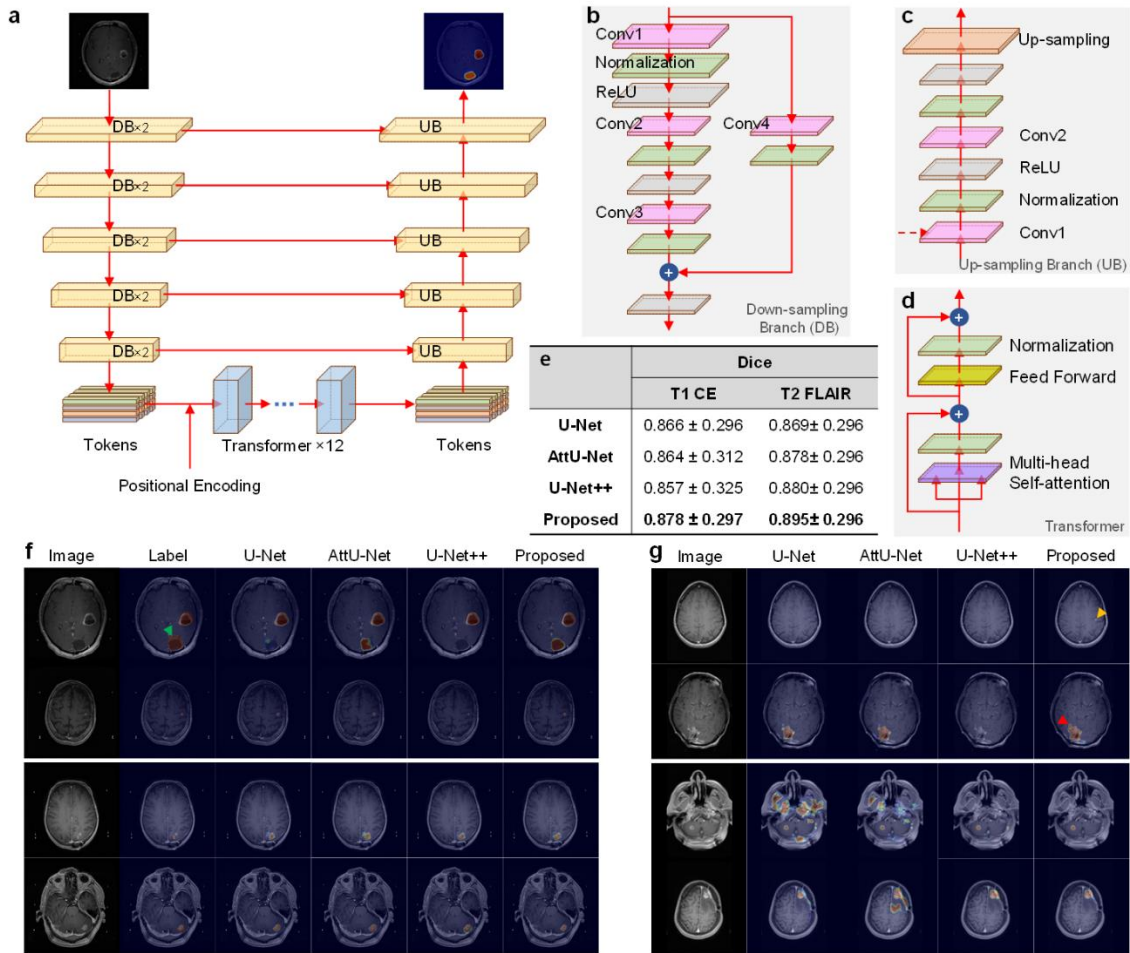


Fig. 2: Proposed brain tumor segmentation network. (a) The proposed segmentation network consisting of the four components: the down-sampling branch, up-sampling branch, transformer bottleneck, and skip connections for the U-net; (b) and (c) the down-sampling and up-sampling branches respectively; (d) the transformer used as the bottleneck in the U-net; (e) quantitative comparison between the proposed segmentation network and three competing brain tumor segmentation networks; (f) visual comparison of validation results between the proposed segmentation network and three competing segmentation networks (the two top rows show T1 CE results, while the two bottom rows show T2 FLAIR results); and (g) visual comparison of results without tumor contour information (the two top rows show T1 CE results, while the two bottom rows show T2 FLAIR results).

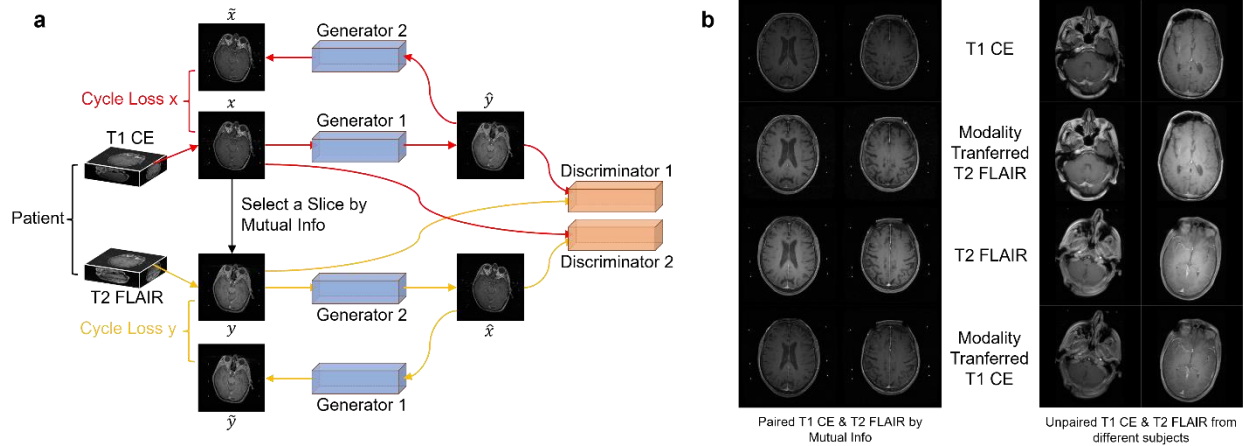


Fig. 3: Proposed cycleGAN for modality transfer. (a) The schematic of the cycleGAN consisting of two generators and two discriminators, where Generator 1 transforms T1 CE to T2 FLAIR, and Generator 2 generates T2 FLAIR from T1 CE. In the training process, mutual information is used to find the most similar slice from the corresponding modality scan of the same patient for weakly supervised learning; and (b) representative modality transferred results, where the first row shows the original T1 CE images, the second row gives the modality transferred T2 FLAIR images from the first row, the third row shows the original T2 FLAIR images, and the fourth row gives the modality transferred T1 CE images from the third row. The left two columns present the validation results, and the T2 FLAIR images are the most similar images with the T1 CE images in the same column. The right two columns present the modality transferred results on two subjects with only one modality, where the top two rows show a subject with T1 CE image and their corresponding modality transfer result, and the bottom two rows show a subject with T2 FLAIR image and their corresponding modality transfer result.

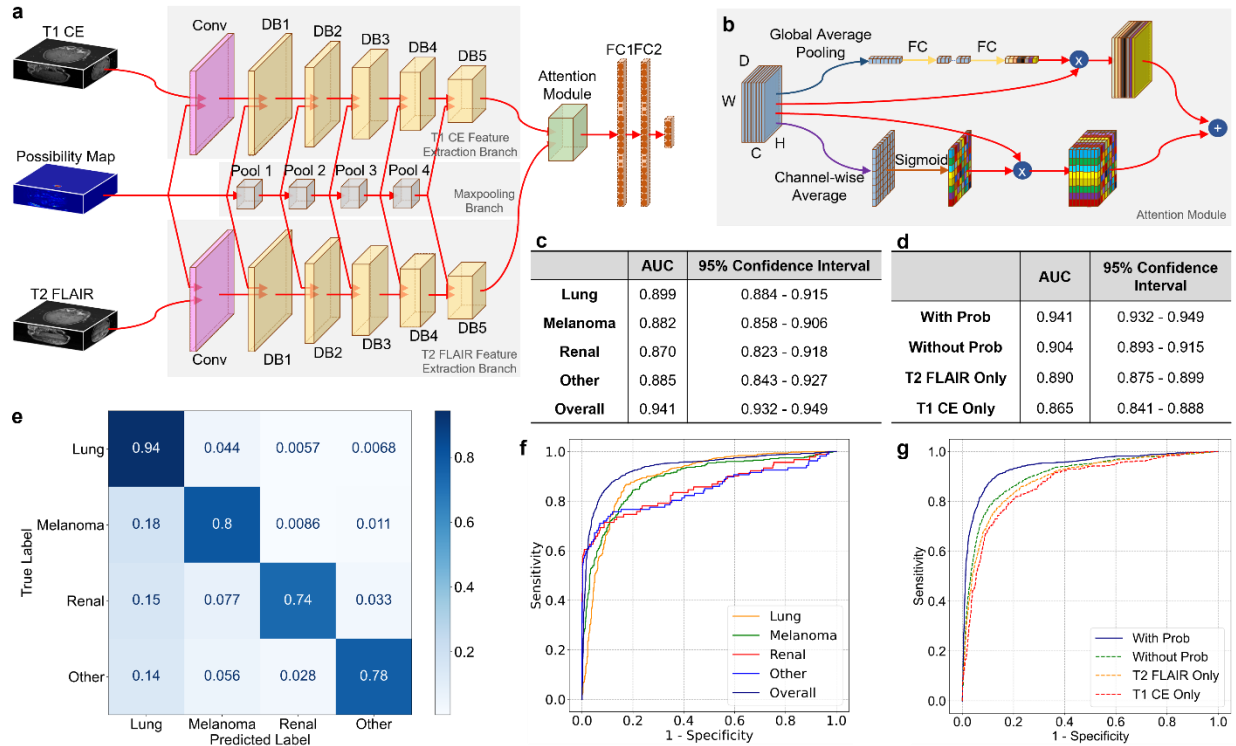


Fig. 4: Proposed brain metastases classification network and its diagnostic performance.

(a) The proposed classification network consisting of two feature extraction branches, where the possibility maps are gradually down-sampled via 3D maximum pooling and concatenated to the features from the two branches. There is an attention module to combine features extracted from T1 CE and T2 FLAIR branches. Then, two fully connected layers are used to generate the final classification outcome; (b) the attention module consisting of a channel attention branch and a spatial attention branch (in the channel attention branch, feature maps are first converted into vectors via 3D global averaging, then two fully connectivity layers calculate the weight for each channel, and finally features maps are channel-wise multiplied by channel weights. In the spatial attention branch, feature maps are first channel-wise averaged, the weight in each voxel is determined via sigmoid activation, and finally features maps are voxel-wise multiplied by weights. The outputs of channel-attention and spatial attention branches are element-wise added to form new feature maps); (c) the classification results; (d) the ablation study results (“With Prob” shows the overall result, “Without Prob” shows the result without adding possibility

maps; “T2 FLAIR Only” shows the result only using T2 FLAIR images for the classification, and “T1 CE Only” shows the result only using T1 CE images for the classification); (e) the confusion matrix for the four-class classification; (f) the ROC curves; and (f) the ROC curves in the ablation study.

Supplementary Table 1 Structure of the proposed segmentation network

Down-sampling block		Segmentation network	
Layer name	Structure	Layer name	Structure
Conv1	1×1, s=1, p=0, in_ch=a, out_ch=b	Conv1	3×3, s=1, p=1, in_ch=1, out_ch=32
Group normalization	num=32, ch=b	DB1_1	a=32, b=32, c=32, d=2
Conv2	3×3, s=d, p=1, in_ch=b, out_ch=b	DB1_2	a=32, b=32, c=64, d=1
Group normalization	num=32, ch=b	DB2_1	a=64, b=64, c=64, d=2
Conv3	1×1, s=1, p=0, in_ch=b, out_ch=c	DB2_2	a=64, b=64, c=128, d=1
Group normalization	num=32, ch=b	DB3_1	a=128, b=128, c=128, d=2
Conv4	1×1, s=d, p=0, in_ch=a, out_ch=c	DB3_2	a=128, b=128, c=256, d=1
Group normalization	num=32, ch=b	DB4_1	a=256, b=256, c=256, d=2
Up-sampling block		DB4_2	a=256, b=256, c=512, d=1
		DB5_1	a=512, b=512, c=512, d=2
Layer name	Structure	DB5_2	a=512, b=512, c=1024, d=1
Conv1	3×3, s=1, p=1, in_ch=a, out_ch=b	Conv2	3×3, s=1, p=1, in_ch=1024, out_ch=768
Group normalization	num=32, ch=b	Transformer x 12	-
Conv2	3×3, s=d, p=1, in_ch=b, out_ch=b	Conv3	3×3, s=1, p=1, in_ch=768, out_ch=1024
Group normalization	num=32, ch=b	UB1	a=2048, b=512
Upsampling	scale=2	UB2	a=1024, b=256
Transformer		UB3	a=512, b=128
		UB4	a=256, b=64
Name	Structure	UB5	a=128, b=32
Head	12	Conv4	3×3, s=1, p=1, in_ch=32, out_ch=2
Hidden dimension	768		
Feed forward fully connected layer 1	in_dim=768, out_dim=768*4		
Feed forward fully connected layer 2	in_dim=768*4, out_dim=768		

Supplementary Table 2 Structure of the proposed classification network

Classification network	
Layer name	Structure
Conv1	3×3×3, s=2, p=1, in_ch=2, out_ch=32
DB1	a=33, b=32, c=32, d=(2,2,2)
DB2	a=33, b=32, c=64, d=(1,2,2)
DB3	a=65, b=64, c=64, d=(2,2,2)
DB4	a=65, b=64, c=128, d=(1,2,2)
DB5	a=129, b=128, c=128, d=(2,2,2)
Attention module	FC1: in_dim=256, out_dim=16 FC2: in_dim=16, out_dim=128
FC1	in_dim=256*8*8*8, out_dim=128
FC1	in_dim=128, out_dim=4